Investigation of the oxygen storage capacity behaviour of three way catalysts using spatio-temporal analysis

Ciaran Coney[a], Christopher Hardacre[b], Kevin Morgan[a], Nancy Artioli[a], Andrew P.E. York[c], Paul Millington[c], Amy Kolpin[c], Alexandre Goguet[a],*

[a] School of Chemistry and Chemical Engineering, David Keir Building, Stranmillis Road, Queen's University Belfast, Belfast, BT9 5AG, UK
[b] School of Chemical Engineering and Analytical Science, University of Manchester, Manchester, M13 9PL, UK
[c] Johnson Matthey Technology Centre, Blounts Court, Sonning Common, Reading RG4 9NH, UK

ABSTRACT

A transient lean-rich switching method has been developed in conjunction with the spatially resolved capillary inlet mass spectrometry (SpaciMS) technique using CO oxidation as a probe reaction. This has allowed in-situ spatiotemporal mapping of gaseous species and temperature profiles inside the channels of commercial three way $1\%Pd/0.07\%Rh/Al_2O_3/Ce_xZr_{1-x}O_2$ and $3\%Pd/Al_2O_3$ monolith catalysts. The identification of the spatio-temporal reactant conversion, intermediate and product formation, as well as the associated heat evolution, has helped in the elucidation of reaction sequences and furthermore, the postulation of reaction mechanisms, both axially and temporally inside the monolith catalyst. Intriguingly in this work, the SpaciMS technique has provided previously unobserved insights into an apparent excess OSC-like behaviour of the $3\%Pd/Al_2O_3$ catalyst, where excess CO conversion is detected under rich CO oxidation conditions in the presence of water. It has been demonstrated that the water gas shift reaction is insufficient to account for the excess CO conversion in this work, therefore a $Pd(OH)_x$ surface species is hypothesised to be acting in the same way as an oxygen storage component under rich conditions.

1. Introduction

Globally spark ignition (petrol) engines account for approximately 80% of the passenger car fleet [1] consequently contributing significantly to greenhouse gas emissions, tropospheric ozone formation and photochemical smog formation via vehicle emissions [2]. The accumulation of vehicle derived CO emissions in urban areas is an additional health concern, particularly due to its link with cardiovascular disease and angina [3,4]. Petrol powered vehicles have been shown to emit relatively high concentrations of CO in relation to alternative fuel vehicles, owing to the fact that spark ignition engines operate at low air to fuel ratios to prevent excessive exhaust temperatures [5]. As a result of the growing concerns regarding local air quality in many areas, coupled with steadily increasing vehicle use, the implementation of increasingly stringent vehicle emission standards [6–8] as well as incentives for hybrid and electric vehicles [9], have been promoted as potential solutions to the growing vehicle emission problem.

Petrol powered vehicles generate a mixture of CO, CO_2, H_2O, N_2O, H_2, NH_3, NO_x (NO, NO_2) and unburned hydrocarbons (C_xH_y) during spark ignition in the combustion chamber of the engine. CO, NO_x and

C_xH_y represent the major unwanted emissions, which for the past 50 years, have been conventionally abated from the vehicle exhaust stream via a catalytic converter employing a Three-Way Catalyst (TWC) [4]. Since the 1970s, TWCs have utilised platinum group metals (PGMs) Pd, Pt and Rh supported on various metal oxides, typically with significant PGM loadings [10], to bring about the simultaneous oxidation and reduction of carbon and nitrogen oxide species respectively [4,11], though large metal saving has been achieved as the technology has matured. This is achieved by dynamic cycling between lean (stoichiometric excess of oxygen) and rich (stoichiometric deficit of oxygen) exhaust conditions, at a typical frequency of 1 Hz [12]. Ideally, under lean conditions, carbon sources are completely oxidised to CO_2 and H_2O via reactions on Pd and/or Pt, whilst under rich conditions reduction of NO to N_2 occurs on Rh and/or Pt.

Ceria based promoters are often added to the catalyst in order to introduce an Oxygen Storage Component (OSC), permitting excess oxygen to be stored in the form of CeO_2 under lean conditions, which can be subsequently accessed by CO and C_xH_y under oxygen deficient conditions [13]. The greater CO and C_xH_y emissions, produced by the engine during the rich fluctuations, are oxidised by a combination of
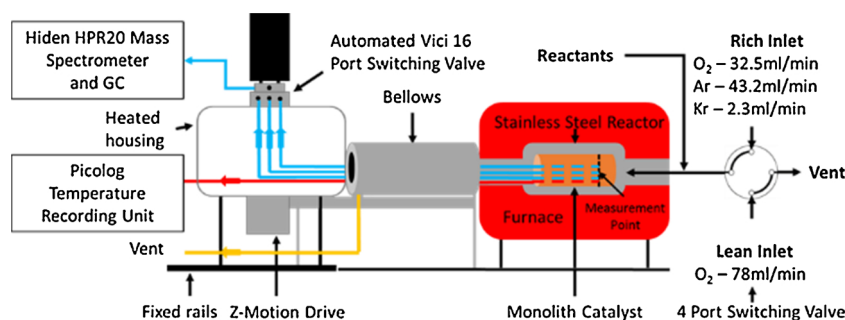
Fig. 1. SpaciMS setup as utilized during lean-rich experimental switching tests.

reactions with adsorbed O_2 and oxygen stored in the form of either CeO_2 or PdO. Steam Reforming (SR) and Water-Gas Shift Reactions (WGSR) also contribute to the removal of CO and C_xH_y, owing to the high H_2O concentrations present in the exhaust stream [14].

The dynamic operating conditions to which TWCs are subjected to, as part of the petrol powered vehicle emission abatement system, dictates that careful consideration must be taken in selecting the most appropriate analysis technique when investigating TWCs. Steady state analysis is an approach commonly employed to investigate global catalytic performance, in which all state variables are maintained at constant values at the reactor inlet whilst the reactions proceed. Although proven to be a useful analysis technique for many catalytic applications, the inherent simplicity and low time resolution of the technique can mean that important mechanistic and kinetic information may be overlooked [15,16]. Regardless of the potential drawbacks, steady state analysis has provided useful insights into various aspects of the TWC catalyst performance, for example the influence of the substrate on conversion efficiency [17], effect of fuel type on non-criteria pollutant abatement [18] and impact of inlet gas concentrations and catalyst formulation on catalyst activity [19,20]. In contrast, transient kinetic analysis overcomes some of the limitations of the steady state approach by assessing the response of a perturbed system in order to identify reaction intermediates and yield micro kinetic information. The oscillatory operating nature of the TWC abatement system requires transient analysis to fully assess the catalytic performance under realistic conditions. CO oxidation is often used as a probe reaction in transient analysis, owing to its ability to quantify OSC capacity and identify mechanistic pathways. Various transient analysis techniques have been employed to investigate catalytic CO oxidation reactions, including pulse injection [21–25], temporal analysis of products (TAP) [15,16,26,27] and SSITKA [28], however the majority of these techniques focus on end-pipe analysis of powdered catalysts. The evolution of reactions occurring inside monolith catalysts has also been conventionally investigated using end-pipe analysis, where the resultant gas at the outlet of the monolith is sampled and analysed by a number of techniques including Gas Chromatography (GC), Mass Spectrometry (MS) and Fourier Transform Infrared spectroscopy (FTIR) [29]. Nevertheless by employing such analysis techniques, crucial intra-catalyst information is often lost within the monolith, especially regarding reaction profiles, intermediate formation, catalyst deactivation, reaction pathways and temperature evolution. To overcome such limitations a number of spatially resolved analysis techniques employing physical measurement probes have been developed, including fixed bed applications using IR, MS or GC analysis [30–35], monolith catalyst testing using spatially resolved capillary-inlet mass spectroscopy (SpaciMS) [36–38] modified with IR [39,40], or applied to foams [41], and other spatially resolved techniques including catalytic plate reactors [42,43] stagnation flow reactors (SFR) [44], scanning mass spectrometry (SMS) on microstructures [45,46], and other SpaciMS like techniques [47–49]. Although the insertion of physical probes can be considered invasive in some configurations, it has been shown via 3D CFD modelling that the probes can be considered non-invasive under

specific conditions and configurations i.e. orientating the probe in the corner of the monolith channel, minimising probe diameter and capillary suction flow rate, and maximising channel flow rate [38]. A comprehensive summary of the spatially resolved techniques currently employed can be found in literature [1,29]. In the present work, the main objective was to develop a transient experimental cycling methodology, capable of spatially and temporally mapping the gaseous reaction profiles occurring inside washcoated monolith cores during lean-rich transient operation. Similar work has been reported elsewhere previously [50,51]. Herein, the SpaciMS technique was employed to probe a central monolith channel for gaseous species concentrations and temperature, using TWCs. The technique was validated using CO oxidation reactions in both the presence and absence of H_2O, shedding light into processes such as carbon deposition, oxygen storage, re-oxidation of the catalyst and contribution of the WGSR to CO conversion. The information gained was ultimately used to hypothesise spatio-temporal reaction network maps, thus giving an insight into the sequence of physical and catalytic processes occurring on TWCs during a transient lean-rich cycle.

2. Experimental

The SpaciMS approach employed in this work has been adapted from previous work carried out at Queen's University Belfast [37,52,53]. In brief the SpaciMS setup consists of various major components including a mass spectrometer, gas sampling unit, tubular furnace, temperature interface, *z*-motion drive unit and stainless steel reactor with an additional two-way VICI switching valve added to the inlet stream, as detailed in Fig. 1. The stainless steel reactor (I.D. ca. 20 mm, length 200 mm) was positioned centrally inside a 1 m split tube Carbolite furnace, equipped with a Eurotherm controller. Typically monolith cores were placed inside the stainless steel reactor allowing horizontal gas flow through the open ended monolith faces. The monolith cores were wrapped with insulation of ca. 2 mm thickness to minimise bypassing of the gas. Gas composition was sampled via a 220 μm O.D. open ended fused silica capillary (Polymicro Technologies) connected to a Hiden HPR20 quartz inlet capillary quadrupole mass spectrometer. Gas temperature was recorded via a 250 μm O.D. type K thermocouple (Omega), and both probes were inserted inside the monolith cores in radially central adjacent channels, as shown in Fig. 2.

The monolith cores were rotated so that the channel walls were 45° to the horizontal and vertical axes, meaning that capillaries and thermocouples are positioned in the corner of the channel, demonstrated computationally to be the least invasive configuration by Hettel et al. [48].

Although other specific invasive cases have been shown to exist, dependent on probe geometry, probe position, channel geometry, channel flow rate, capillary suction rate and reaction profile, such invasive instances have been minimised in this work by using a similar non-invasive configuration as detailed previously [37,52,54]. The probes were translated axially inside the monolith channels via a movable z-motion linear stage controlled by a Thorlabs APT Microstepping
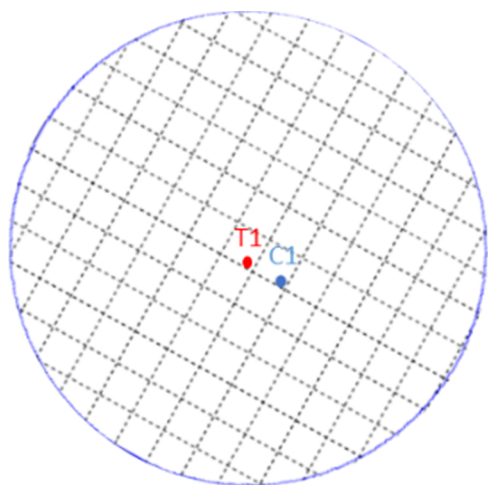
Fig. 2. Representative radial distribution of measurement probes at inlet face of monolith core.

Controller (BSC101). The oscillation of the 2 way VICI valve between lean and rich conditions was controlled by an automated MATLAB program in which the time per feed stream and the number of switches were predetermined. Water vapour was supplied via a controlled evaporation and mixing system (Bronkhorst CEM, Model W-101A), allowing the delivery of precise quantities of water vapour to the reactor.

In all, three catalysts supported on monolithic ceramic substrates were supplied by Johnson Matthey; $1\%Pd/0.07\%Rh/Al_2O_3$ (non-OSC TWC), $1\%Pd/0.07\%Rh/Al_2O_3/Ce_xZr_{1-x}O_2$ (TWC) and $3\%Pd/Al_2O_3$ (non-TWC). The TWC consists of PGMs Pd and Rh, supported on a combination of Al_2O_3 and $Ce_xZr_{1-x}O_2$, culminating in a $1\%Pd/0.07\%$ $Rh/Al_2O_3/Ce_xZr_{1-x}O_2$ catalyst washcoated on a cordierite substrate. The addition of $Ce_xZr_{1-x}O_2$ compared to the non-OSC TWC catalyst adds an oxygen storage component to the TWC catalyst. The non-TWC consists of Pd supported on Al_2O_3, washcoated on a cordierite substrate. The washcoated monolith cores (400 cpsi), O.D. ca. 17.2 mm, and length ca. 102 mm, were positioned inside the sealed stainless steel reactor.

CO oxidation was used as a probe reaction in order to develop a transient switching methodology capable of spatiotemporally mapping the reaction pathways occurring inside monolith cores. Two distinct reaction conditions were screened: dry and wet. The dry feed gas mixture consisted of a constant, common gas flow of 2.2 vol% CO balanced in Ar, supplemented with alternating lean and rich gas flows consisting of 1.56 vol% and 0.65 vol% O_2 respectively. The lean and rich gas streams were balanced in Ar and Ar/Kr respectively. The wet feed gas mixture contained an additional 5 vol% H_2O in the constant, common gas flow stream labelled 'Reactants' in Fig. 1. The feed was cycled between rich and lean conditions at a frequency of 0.025 Hz employing a steady state furnace temperature of 250 °C in order to scan axial positions between 0–40 mm of the monolith cores. Each core was subjected to a total gaseous flow rate of 5000 mL min^{-1} (STP), corresponding to a space velocity of ca. 90,000 h^{-1} at an axial position of 40 mm. The temperature gradient between the two adjacent central channels was found to be negligible, thus the assumption of equality between the gas temperatures of adjacent central channels can be justified. Blank control experiments were conducted to assess any contribution of homogenous reactions and none were observed for the conditions studied herein.

Prior to an experimental run, capillary C1 and thermocouple T1 were axially positioned 3 mm in front of the inlet of the monolithic core so as to record the inlet concentrations. Each monolithic catalyst core was pre-treated by firstly subjecting it to 10 vol% O_2 at 250 °C in a total gas flow of 1000 mL min^{-1} at STP for a period of 1 h. This ensured the replenishment of any oxygen storage component and returned the catalysts to a reference oxidation state at the beginning of each
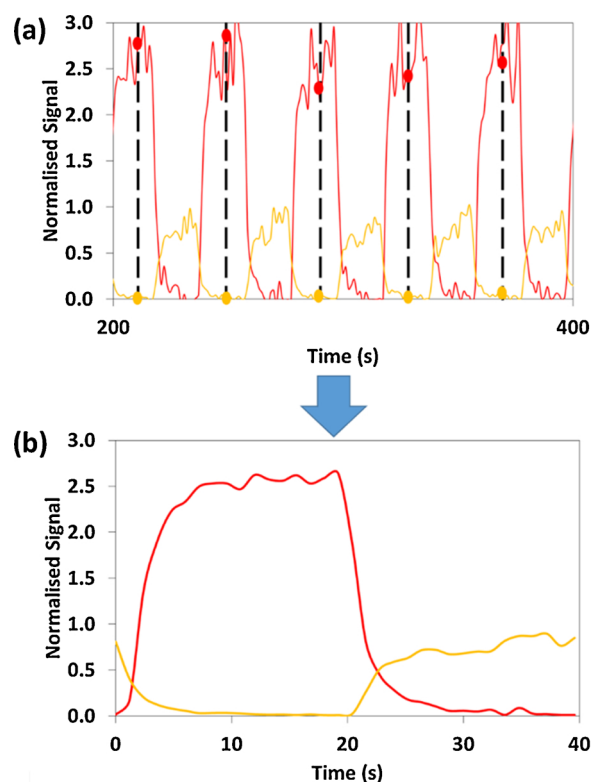

Fig. 3. (a) Normalized mass spectrometer signals for CO (red) and O_2 (gold) as a function of time and (b) resultant normalized signal averaged plot for CO and O_2 (For interpretation of the references to colour in this figure legend, the reader is referred to the web version of this article).

experiment. Each core was then exposed to 100 vol% Ar at 250 °C in a total gas flow of 5000 mL min^{-1} for a period of 1 h in order to achieve a steady baseline value.

The reaction profiles were produced by positioning probes at axial measurement positions of 1, 2.5, 5, 7.5, 10, 12.5, 15, 20, 25, 30, 35, and 40 mm along the channel length. During the cycling routine occurring at each axial position, the catalyst was initially exposed to lean conditions for 20 s, thereafter cycled between rich and lean conditions every 20 s, finishing with the catalyst exposed to lean conditions at the end of the 50 switches. The catalyst was exposed to lean conditions as the probes were translated axially to their new positions, thus ensuring that the catalyst and oxygen storage component were being returned to a fully oxidised reference condition before the beginning of each switching routine. For each axial position, a signal averaging approach was applied to each species, with the purpose of increasing the signal to noise ratio for all of the gas composition and temperature data. Fig. 3 (a) gives an example of how the signal averaging approach is applied over 5 cycles, where the CO and O_2 signals existing at complimentary time points on each cycle (red and gold dots), were added together, and an average value was calculated for each species at each time instance of a cycle. The resultant plot for the signal averaged data over 40 switching cycles is displayed in Fig. 3(b). The first 10 switches were discarded in order to ensure data integrity. This process was also applied to Kr, CO_2, H_2O and H_2 species signals as well as carbon, oxygen and hydrogen atom balances reported in this work. The signal averaged plot in Fig. 3(b) was produced for each axial position, giving rise to a number of axial slices detailing gaseous species conversion and temperature evolution over the 40 s cycle time. The axial slices in Fig. 4(a) were combined into 3-Dimensional plots for each individual species, where either conversion, yield or temperature (*y*-axis) is plotted as a function of switching time (*x*-axis) and axial position inside the channel (*z*-axis), detailed in Fig. 4(b). Although useful in terms of
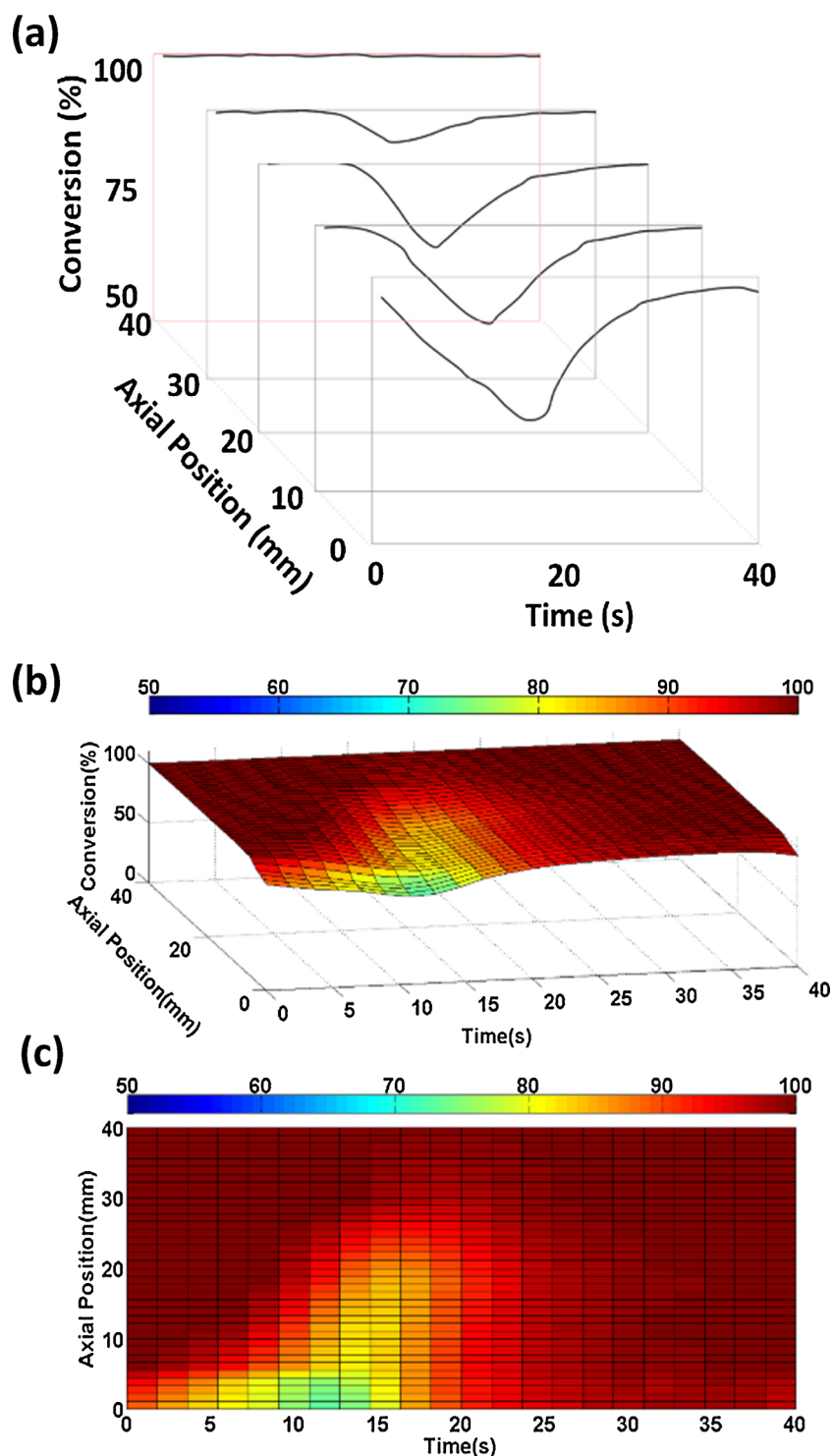
Fig. 4. (a) CO conversion as a function of time at axial slices of 0, 10, 20, 30 and 40 mm (b) 3-Dimensional spatiotemporal representation of CO conversion and (c) 2-Dimensional spatiotemporal representation of CO conversion, for the 0.025 Hz lean-rich cycling CO oxidation reaction occurring on a TWC carried out at a furnace temperature of 250 °C.

simultaneously visualizing temporal and spatial reaction profiles, 2-Dimensional 'birds eye' plots exemplified in Fig. 4(c), have proven to be a better tool for interpreting the spatiotemporal reaction profiles.

The 2-Dimensional plots detail the spatial (*y*-axis) and temporal (*x*-axis) evolution of conversion, yield or gaseous temperature, with the magnitude of the dependent variable being denoted by a colour scale. All subsequent spatiotemporal plots contained in this work have been constructed using this method, and aid in the identification of potential

reaction pathways.

3. Results and discussion

Initially, exploratory tests were conducted to determine the most appropriate cycling efficiency, ensuring that a sufficient relaxation period was realised after each perturbation, therefore allowing the inlet gas concentrations to breakthrough. To achieve this, the TWC catalyst
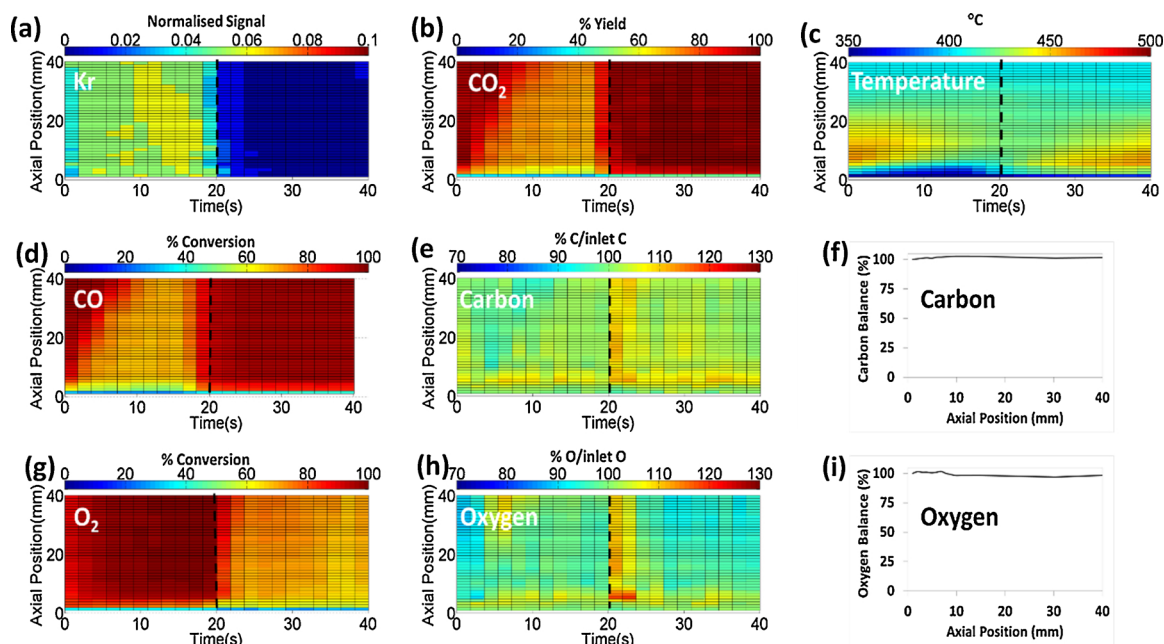
Fig. 5. Spatiotemporal evolution of (a) $Kr_{(g)}$, (b) CO_2 yield, (c) gas temperature, (d) CO conversion, (e) atomic carbon balance, (g) O_2 conversion, (h) atomic oxygen balance for the lean-rich cycling CO oxidation occurring on the non-TWC catalyst, axial evolution of total (f) carbon and (i) oxygen atom balance per cycle.

was exposed to perturbing Kr and non-Kr containing feeds, where various perturbation frequencies were tested until full Kr breakthrough was attained. Kr was chosen due to its relative inertness leading to a lack of interaction with the monolith wash coat or substrate. As demonstrated by Fig. S1, a cycling frequency of 0.025 Hz was found to offer a suitable trade-off between high frequency perturbations and a sufficient relaxation period, thus has been employed in all subsequent experimental tests detailed in this work.

3.1. Dry feed

The first test of the experimental methodology was aimed at tracing the reaction profiles and ascertaining the oxygen storage capacity of both catalysts. The non-TWC monolith core was initially subjected to the dry feed reaction mixture. The resulting spatiotemporal plots are displayed in Fig. 5 for the Kr tracer (a), gaseous temperature (c), the conversion profiles of CO (d) and O_2 (g) and the respective carbon and oxygen atomic balances (e and h) and the respective time averaged atomic carbon (f) and oxygen (i) balances at each axial position. Finally, Fig. 5(b) reports the spatiotemporal CO_2 yield profile.

The spatiotemporal Kr gas profile, Fig. 5(a), enabled the identification of the lean and rich periods of the cycle, where the presence of Kr (0–20 s) and the absence of Kr (20–40 s), represents rich and lean inlet conditions respectively. During a switching cycle at a fixed axial position the Kr gas profile was used as a calibration tool where the varying inlet oxygen concentration could be identified at each time instance during the 40 s cycle. This permitted the theoretical stoichiometric CO conversion, O_2 conversion and CO_2 yield to be calculated at each time instance during the cycle, based on the stoichiometry of the CO oxidation reaction and the inlet feed concentrations. The calculated stoichiometric CO conversion is displayed in Fig. 6(a), with the experimental CO conversion occurring over the non-TWC and TWC, reported in Fig. 6(b) and (c), respectively.

Further information regarding the potential deposition of carbon species and the origin of the oxygen utilized in the oxidation of CO to CO_2 has been derived from the spatiotemporal data. By comparing the predicted stoichiometric conversions and yields to the experimentally recorded conversions and yields, it is possible to identify both the spatial and temporal regions within the catalytic monolith core where
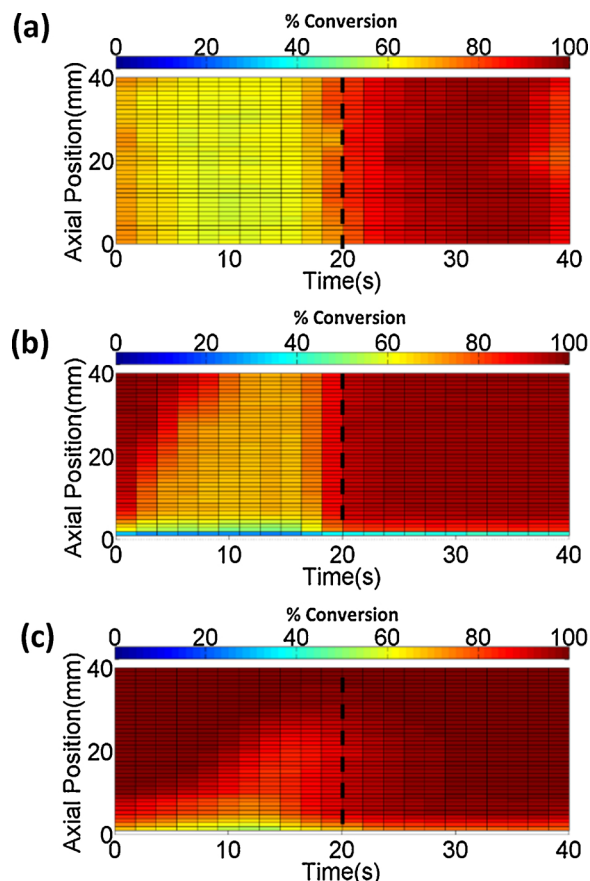

Fig. 6. Spatiotemporal CO conversion during a lean-rich cycle (a) as predicted via inlet feed and stoichiometry, (b) as experimentally recorded for the TWC, (c) as experimentally recorded for the non-TWC.

conversions/yields are in excess or in deficit of the predicted stoichiometric values. For each respective species, spatiotemporal contour plots detailing the difference between the predicted stoichiometric and
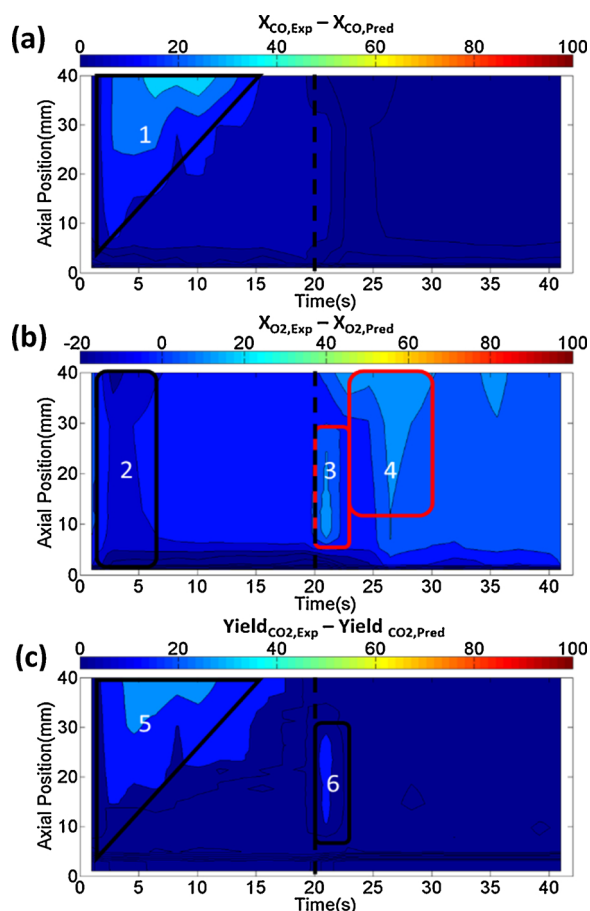
Fig. 7. Spatiotemporal difference between experimental and predicted (a) CO conversion (b) O_2 conversion (c) CO_2 yield for lean-rich CO oxidation reaction using non-TWC catalyst.

experimentally measured conversions ($X_{Exp} – X_{Pred}$) and yields ($Yield_{Exp} – Yield_{Pred}$) have been produced (Fig. 7).

The contour plots enclose spatiotemporal regions signifying similar conversion/yield differences, where the total measureable scale is divided into 10 equally spaced zones, with a specific colour representative of each zone. Fig. 7(a) displays the spatiotemporal CO conversion in excess of stoichiometry, Fig. 7(b) displays the spatiotemporal O_2 conversion in excess of stoichiometry and Fig. 7(c) displays the spatiotemporal CO_2 yield in excess of stoichiometry. Quantitatively from Fig. 7(a), excess CO conversion is achieved under rich conditions (region 1), which is also validated by the stoichiometric excess of CO_2 formed (region 5) in Fig. 7(c). The extra CO conversion can be explained by the reaction of CO with stored oxygen on Pd particles, where oxygen is stored as PdO under oxidising conditions. The oxidation of Pd to PdO and subsequent reaction of PdO with CO has been demonstrated to occur at temperatures similar to those experienced in this work, via TPO studies carried out by Cordi and Falconer [55]. Fig. 7(b) (region 4) further validates this hypothesis by highlighting additional O_2 conversion observed under lean conditions. An unexpected deficit in O_2 conversion is detected directly after the switch from lean to rich conditions (region 2), as under an oxygen deficient environment it would be expected that 100% of the O_2 would be converted. However it appears that a portion of the incoming CO is reacting preferentially with oxygen stored as PdO. This theory is backed up by the excess oxygen present in the gas phase, Fig. 5(h) (Fig. 7(b) region 3), where the excess oxygen is attributed to oxygen originating from PdO. Excess O_2 conversion is also observed directly after the switch from rich to lean conditions, Fig. 7(b) (region 3), confirming the existence of another oxidation process. This is surmised to be linked with excess CO_2 formed, Fig. 7(c) (region 6), thus indicating the existence of an additional carbon source. By interpreting the carbon balance in Fig. 5(e), which details the carbon present in the gas phase at a point in time and space, as a percentage of the inlet carbon present in the gas phase, Eq. (1), a deficit of carbon is observed in the gas phase at a spatiotemporal instance corresponding to regions 1 and 5. Therefore it has been hypothesised that a carbon species has been deposited on the catalyst surface, thought either to be in the form of adsorbed $CO_{(ad)}$ or another deposited carbon species, possibly $C_{(s)}$ formed via the Boudouard reaction [56]. A darkening of the surface of the catalyst was observed post reaction, which would indicate a deposition of a carbon species, most likely C(s). The carbon balance, Fig. 5(f), and oxygen balance, Fig. 5(i), confirm that all carbon and oxygen species are accounted for during the full cycle, at all axial positions.
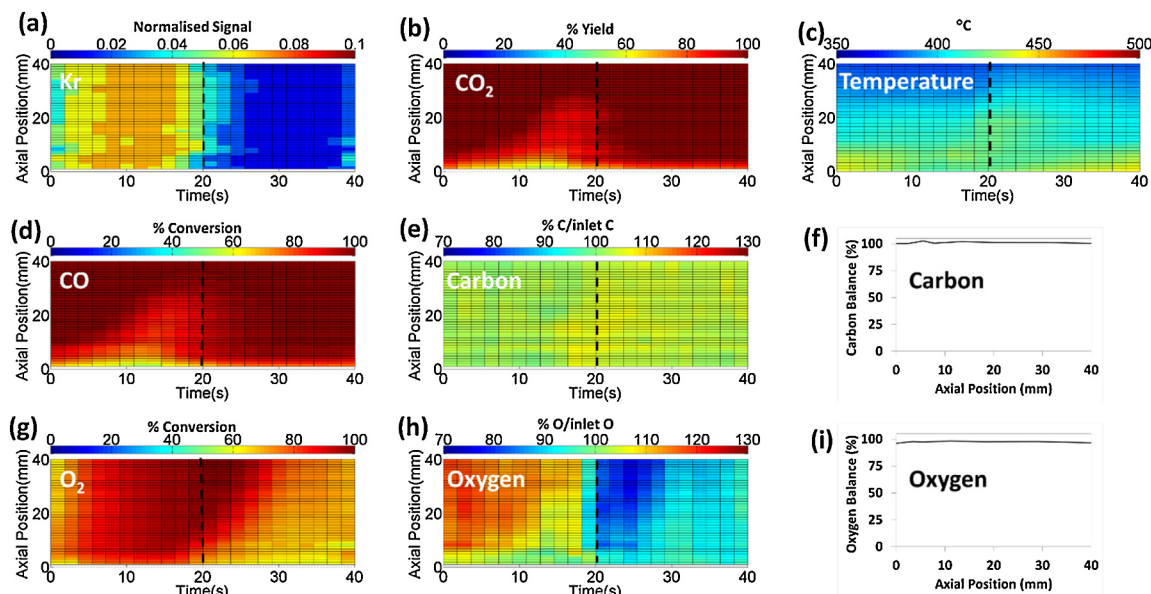

Fig. 8. Spatiotemporal evolution of (a) Kr, (b) CO_2 yield, (c) gas temperature, (d) CO conversion, (e) atomic carbon balance, (g) O_2 conversion, (h) atomic oxygen balance for the lean-rich cycling CO oxidation occurring on the TWC catalyst, axial evolution of total (f) carbon and (i) oxygen atom balance per cycle.
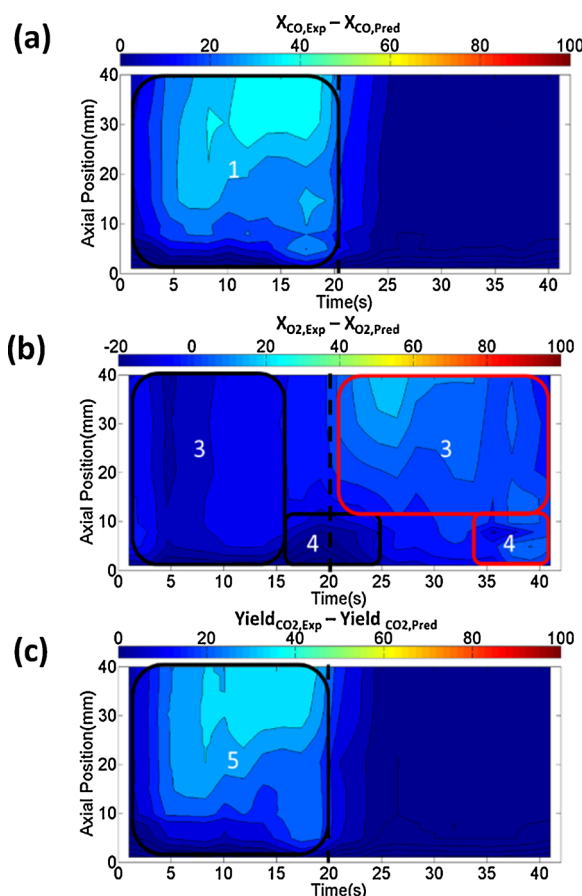
Fig. 9. Spatiotemporal difference between experimental and predicted (a) CO conversion, (b) O_2 conversion, (c) CO_2 yield for lean-rich CO oxidation reaction using TWC.

$$\left(\frac{C_{(g),t,z}}{C_{(g),t,z=0}} \right) x100 \tag{1}$$

Switching focus to the TWC, Fig. 8 reports the spatiotemporal plots derived from the experimental tests carried out on a 1%Pd/0.07%Rh/Al_2O_3/$Ce_xZr_{1-x}O_2$. Fig. 8(a) reports the spatiotemporal Kr tracer profile; Fig. 8(c) the spatiotemporal gaseous temperature profile; Fig. 8(d) and (g) the respective spatiotemporal CO and O_2 conversion profiles; Fig. 8(e) and (h) the respective spatiotemporal carbon and oxygen atomic balances; Fig. 8(f) and (i) the respective time averaged atomic carbon and oxygen balances at each axial position and Fig. 8(b) reports the spatiotemporal CO_2 yield profile. Fig. 8(d) clearly highlights the additional effect of the OSC on the CO oxidation reaction, via excess CO conversion and CO_2 yield identified by regions 1 and 5 in Fig. 9(a) and (c), respectively.

It was initially surmised that the perceived excess CO conversion could be at least partially accredited to adsorption of CO onto the surface of the catalyst. However the carbon balance in Fig. 8(e) shows that the carbon present in the gas phase throughout the duration of the

cycle is ca. 100% at all axial positions. This suggests that the CO ↔ $CO_{(ad)}$ process is at equilibrium at all positions and time instances during the reaction, therefore no additional accumulation of $CO_{(ad)}$ is experienced on the surface of the catalyst. Fig. 8(f), detailing the average carbon mass balance per axial position, reinforces the hypothesis that the excess perceived CO conversion is not due to $CO_{(ad)}$. The utilization of gaseous O_2 during the reaction can be divided into 4 regions, reported in Fig. 9(b). Region 4 (red) reports a spatiotemporal instance where the experimental O_2 conversion exceeds the predicted conversion, occurring between axial positions of 0–10 mm and time periods of 35–40 s, therefore existing at the end of the lean phase of the cycle. This excess O_2 conversion can be explained by the deficit in O_2 conversion observed in region 4 **(black)** at the end of the rich phase (0–10 mm, 15–25 s), where the incoming CO reacts with a combination of the adsorbed $O_{2(ad)}$ and the stored oxygen. Thus the deficit in O_2 conversion represents the reaction of CO with CeO_2 and the excess O_2 conversion represents the replenishment of the Ce_2O_3. Region 3 **(black)** represents a time period occurring 4 s after the switch to rich conditions, where the experimental O_2 conversion is less than predicted, indicating that the CO is again reacting with a combination of adsorbed $O_{2(ad)}$ and CeO_2 during the time period 2.5–10 s between axial positions of 0–40 mm. The re-oxidation of the Ce_2O_3 (from the OSC) occurs in region 3 (red) which begins directly at the point of the switch to lean conditions at a time of 20 s, occurring at axial positions greater than 10 mm. An evolution of heat is observed at this spatiotemporal instance, Fig. 8(c), which corresponds with the exothermic re-oxidation of Ce_2O_3 [57]. The apparent increase in O_2 conversion and thus the extent of re-oxidation of the OSC with axial position, is merely a cumulative effect of the re-oxidation of Ce_2O_3. The oxygen mass balance in Fig. 8(h) verifies where and when the gaseous oxygen is utilized during the reaction, whilst Fig. 8(i) confirms that the oxygen mass balance is closed, therefore all gaseous oxygen species are accounted for in the analysis.

The information gained from the spatiotemporal analysis has aided in the identification of reaction pathways existing during the CO oxidation reaction occurring over both catalysts, summarised in Table 1 and 2. The hypothesized reaction pathways are superimposed on the spatiotemporal $X_{CO,Exp}$ and ($X_{O2,Exp}$ – $X_{O2,Pred}$) evolutions in Figs. 10 and 11. Spatiotemporal regions have been ring fenced according to the identified reactions occurring at each instance in time and space.

In brief, the chemical reaction pathways experienced by the TWC under rich conditions (0–20 s) are dominated by the reaction of CO with adsorbed O_2 at the front of the monolith, Fig. 10(a), region 1, gradually transitioning to CO oxidation via stored oxygen towards the back of the monolith represented by the interface of regions 1 and 2 in Fig. 10(a). A deficit in gas phase O_2 conversion under rich conditions originates in the front portion of the monolith, Fig. 10(b), region 1, with the most intense deficit occurring directly after the switch from lean to rich conditions when the CO reacts most readily with oxygen stored in the forms PdO and CeO_2 (4–10 s). It should be noted that no reactions occur in region 2 as all CO has been removed prior to the interface of regions 1 and 2. When exposed to lean conditions (20–40 s), the reaction of CO with stored oxygen (PdO or CeO_2) appears to contribute to some extent to the total CO oxidation observed in Fig. 10(b), region 1, (20–25 s), highlighted by the O_2 conversion deficit coupled with the almost 100%

Table 1
Hypothesised reaction network occurring on TWC monolith catalysts for CO/O_2 reaction.

Region	1%Pd/0.07%Rh/Al_2O_3/$Ce_xZr_{1-x}O_2$ (TWC) Reactions
1	$2CO_{(g)} + O_{2(g)} \rightarrow 2CO_{2(g)}$ $CO_{(g)} + 2CeO_{2(s)} \leftrightarrows CO_{2(g)} + Ce_2O_{3(s)}$
1→2	$CO_{(g)} + 2CeO_{2(s)} \leftrightarrows CO_{2(g)} + Ce_2O_{3(s)}$ $CO_{(g)} + PdO_{(s)} \rightarrow Pd_{(s)} + CO_{2(g)}$
2	No reaction
3	$2CO_{(g)} + O_{2(g)} \rightarrow 2CO_{2(g)}$ $O_{2(g)} + 2Ce_2O_{3(s)} \leftrightarrows 4CeO_{2(g)}$ $O_{2(g)} + 2Pd_{(s)} \rightarrow 2PdO_{(s)}$
4	$O_{2(g)} + 2Ce_2O_{3(s)} \rightleftharpoons 4CeO_{2(s)}$ $O_{2(g)} + 2Pd_{(s)} \rightarrow 2PdO_{(s)}$

Table 2

Hypothesised reaction network occurring on non-TWC monolith catalysts for CO/O_2 reaction.

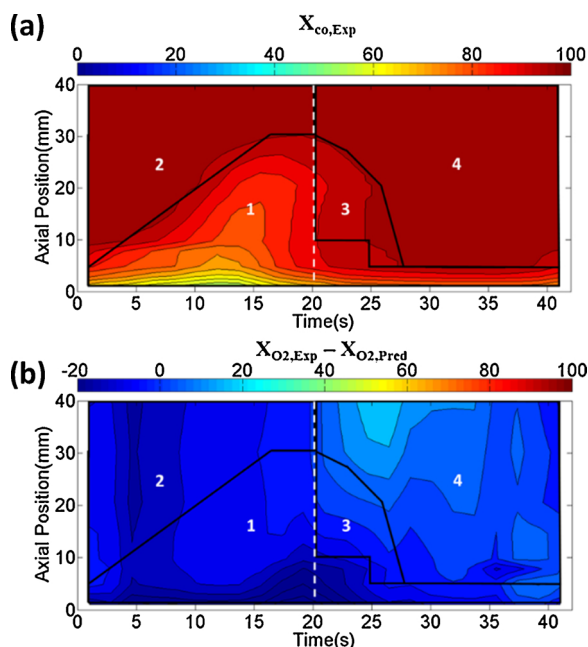| Region	3%Pd/Al_2O_3 (non-TWC) Reactions
1	$2CO_{(g)} + O_{2(g)} \rightarrow 2CO_{2(g)}$
2	$CO_{(g)} + PdO_{(s)} \rightarrow Pd_{(s)} + CO_{2(g)}$ $2CO_{(g)} + O_{2(g)} \rightarrow 2CO_{2(g)}$ $2CO_{(g)} \leftrightharpoons C_{(s)} + CO_{2(g)}$
3	No reaction
4	$O_{2(g)} + 2Pd_{(s)} \rightarrow 2PdO_{(s)}$ $O_{2(g)} + C_{(s)} \leftrightharpoons CO_{2(g)}$ $2CO_{(g)} + O_{2(g)} \rightarrow 2CO_{2(g)}$

Fig. 10. CO oxidation reaction pathway identification on TWC displayed on spatiotemporal plots of (a) experimental CO conversion, (b) difference between experimental O_2 and predicted O_2 conversion.
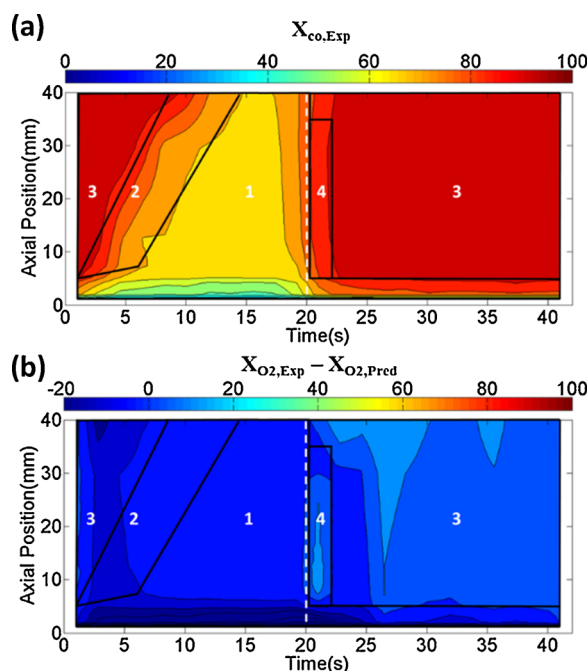

Fig. 11. CO oxidation reaction pathway identification on non-TWC displayed on spatiotemporal plots of (a) experimental CO conversion, (b) difference between experimental O_2 and predicted O_2 conversion.

CO conversion. Progressing axially towards the outlet of the monolith, the O_2 conversion changes from deficient to excess, signified by the transition from region 3 to 4 in Fig. 10(b). This represents the re-oxidation of the ceria support and Pd and also increases with time of lean O_2 exposure until the support is fully replenished.

The reaction pathways attributed to the non-TWC are relatively straight forward in comparison to the TWC. The rich period of operation can be divided into three reaction regions (Fig. 11): region 1 corresponding to the reaction of CO with adsorbed O_2 only; region 2 reflecting the oxidation of CO with adsorbed O_2 and stored oxygen in the form of PdO, as well as carbon deposition via CO disproportionation; region 3 representing spatiotemporal instances during which zero CO oxidation is observed due to the prior total conversion of CO in earlier portions of the monolith corresponding to these time instances. Progressing from rich to lean conditions (20–40 s), the reaction of CO with adsorbed O_2 is the dominant reaction occurring in region 4, Fig. 11, however the addition of excess O_2 under lean conditions also brings about the oxidation of carbon which has been deposited under rich conditions. As more time elapses, all of the deposited carbon is cleaned from the catalyst surface, allowing the remaining O_2 to re-oxidize the reduced Pd, evidenced by the excess O_2 conversion observed.

3.2. Wet feed

The validated spatiotemporal cycling methodology was then applied to CO oxidation reactions occurring in the presence of 5 vol% H_2O in the feed, where the TWC and non-TWC catalytic monolith cores were explored under the same configuration and reaction conditions as those applied to the dry feed. Fig. 12 reports the spatiotemporal CO conversion (a and b), H_2 yield (c and d), and O_2 conversion (e and f) plots obtained from the CO oxidation reactions occurring in the presence of water on both catalysts. As with the dry lean-rich CO oxidation reaction, the predicted stoichiometric rich CO conversion is expected to be 60%, however CO conversions in excess of 60% are detected for both catalysts under rich conditions, Fig. 12(a) and (b). The excess CO conversion occurring on the TWC catalyst can be attributed to reaction of CO with oxygen stored in the form of either CeO_2 or PdO, followed by WGSR indicated by the H_2 production in Fig. 12(c). WGSR is known to occur on ceria supported precious metals [58–60] and H_2 production is only observed when the surface is most likely sufficiently reduced by CO, indicated by the time taken to detect H_2 after the switch from lean to rich conditions. Excess O_2 conversion is observed immediately after the switch from rich to lean conditions, Fig. 12(e), indicative of the re-oxidation of the oxygen storage component as well as reaction with H_2 to form H_2O.

The excess rich CO conversion brought about by the oxygen storage component of the TWC catalyst is expected, however the same cannot be said for the excess CO conversion experienced by the non-TWC catalyst under rich conditions, (0–20 s) Fig. 12(b).

Fig. 13(c) detailing the spatiotemporal CO conversion in excess of stoichiometry, demonstrates that significantly more CO is converted than dictated by stoichiometry under rich conditions.

Quantification of the CO conversion in excess of stoichiometry, for both dry and wet feeds, is displayed as apparent oxygen storage capacity in Table 3. Further details on the determination of the apparent OSC is contained in the ESI. The reduction of palladium oxide particles
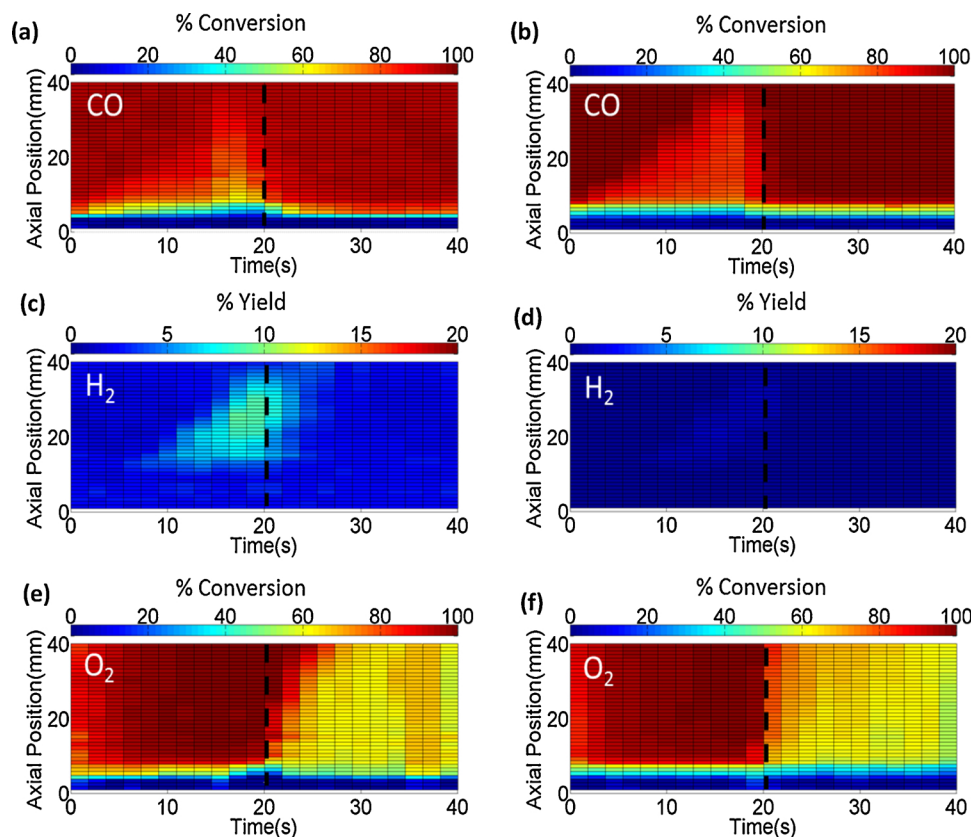
Fig. 12. Spatiotemporal evolution of (a) CO conversion, (c) $H_{2(g)}$ yield and (e) O_2 conversion during the lean-rich CO oxidation reaction occurring on TWC. Spatiotemporal evolution of (b) CO conversion, (d) H_2 yield and (f) O_2 conversion during the lean-rich CO oxidation reaction occurring on non-TWC catalyst.

is known to exhibit different reduction rates in the PdO-particles core and on the surface with the reduction of the surface being significantly faster. Consequently, the apparent oxygen storage capacity is normalized to the amount of surface Pd available in the catalysts. Quantification of the OSC values was carried out by using the inlet molar flows of $CO_{t,z=0}$ and $O_{2,t,z=0}$ at each time instance during the cycle, to predict the expected stoichiometric molar flow of CO at an axial position of 40 mm inside the monolith cores. The difference between the molar flows, CO_{pred} (predicted stoichiometric CO) and CO_{obs} (experimentally observed CO), equates to the CO_{def} (deficient CO) molar flow produced by the excess CO conversion. Owing to a stoichiometric ratio of $2CO:O_2$, the apparent excess molar flow of O_2 ($O_{2,exc}$) consumed in bringing about this additional CO conversion, is calculated as half that of the CO_{def} molar flow. The apparent excess moles of O_2 (excess mol_{O2}) accounting for the excess CO conversion is then calculated via Eqn. 2, where $O_{2,exc}$ at the terminal axial measurement position ($z = 40$ mm) is evaluated at 33 discrete time points using a Δt of 1.21 s. The summation of the excess mol_{O2} at each interval over the duration of a lean-rich cycle, results in the total stored oxygen on the catalyst.

$$mol_{O2,exc} \approx \sum_{i=1}^{33} \frac{(CO_{pred,i}(z=40) - CO_{obs,i}(z=40))\Delta t}{2} \tag{2}$$

Initially it was surmised that the excess CO conversion was attributed to the WGSR [61] however the contribution of the WGSR has been accounted for by calculating the molar quantity of CO required to produce the small amount H_2 observed in Fig. 12(d). Fig. 13(a), detailing the spatiotemporal CO conversion attributed to the WGSR, shows that at any spatiotemporal instance, the maximum CO conversion attributed to the WGSR is less than 5%, thus is not sufficient to

account for the 20% excess CO conversion witnessed under rich conditions, Fig. 13(c). The apparent OSC of the TWC catalyst in the presence and absence of water is approximately equal (5.38 and 4.87, respectively), however this is much greater than that of both the non-OSC TWC and non-TWC catalysts under the same wet and dry conditions.

This is attributed to the ability of the ceria component to readily undergo the Ce_2O_3 to CeO_2 redox reaction during the exposure to alternating oxidizing and reducing conditions. In contrast to this, under wet conditions the non-TWC experiences an apparent OSC corresponding to a value 2.39 times greater than the apparent OSC observed under dry conditions. This promotional CO conversion effect observed in the presence of H_2O is thought to be linked to the availability of Pd at the surface of the catalyst, and this is supported by the results of an independent test carried out on a $1\%Pd/0.07\%Rh/Al_2O_3/ZrO_2$ (non-OSC TWC), Fig. S2. The apparent OSC of the non-OSC TWC is displayed in Table 3, and it has been noted that the apparent dry and wet OSCs of the non-TWC and non-OSC TWC are similar to one another, even though Pd dispersion is markedly different. The discrepancy in Pd dispersion is accounted for by considering only the available surface Pd, dictated by a combination of dispersion and wash coat loading for each catalyst.

The ratio of the apparent OSC with H_2O, to the apparent OSC without H_2O, is equal to 2.07 for the non-OSC TWC and is comparable with the ratio of 2.39 obtained for the non-TWC. The similarity in this ratio indicates that the promotional effect of the water is acting consistently on the Pd sites of both catalysts, denoted by the reaction of H_2O with PdO to form OSC_{add} in Table 4. In contrast the contribution of the ceria component in the TWC catalyst is the dominating factor in determining apparent OSC, ultimately resulting in a ratio of ca. 1 for the
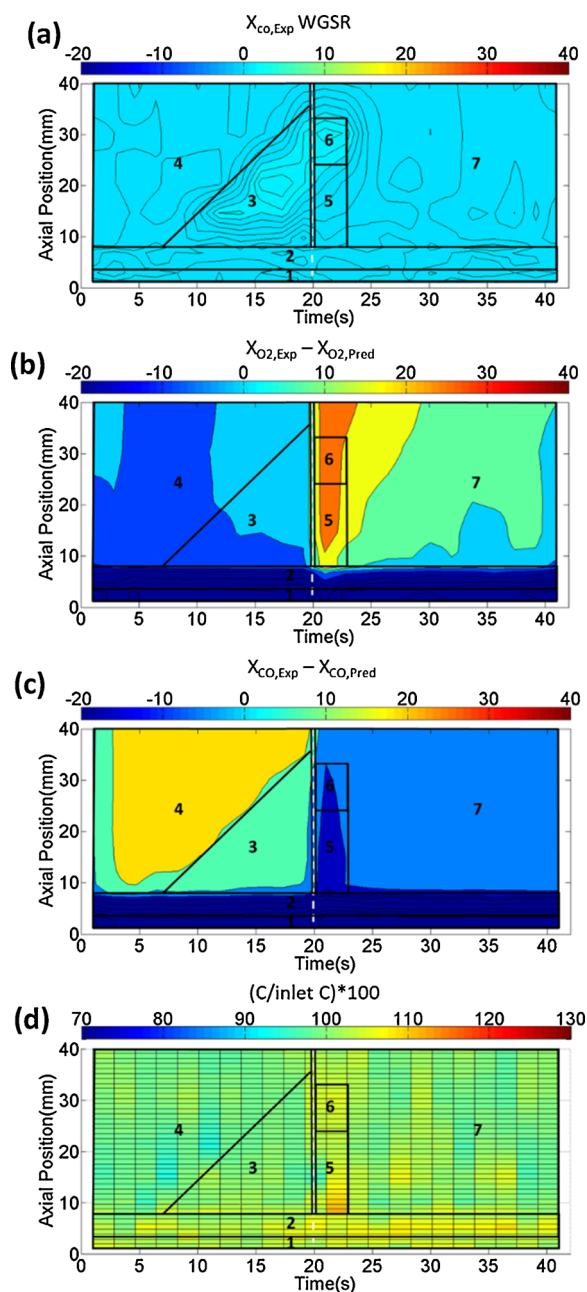
Fig. 13. Spatiotemporal maps detailing (a) experimentally recorded CO conversion attributed to WGSR, (b) difference in experimental and predicted stoichiometric $O_{2(g)}$ conversion, (c) difference in experimental and predicted stoichiometric CO conversion and (d) percentage carbon atom balance based on carbon at the inlet. All maps are based on results obtained from non-TWC tests and include labelled reaction zones as per Table 4.

Table 3
Calculated oxygen storage capacity.

Catalyst	Apparent OSC Without H_2O (mol_O/mol_{Pd})	Apparent OSC With H_2O (mol_O/mol_{Pd})
Non-TWC	0.88	2.12
TWC	4.87	5.38
non-OSC TWC	0.85	1.79

apparent OSC with H_2O, to the apparent OSC without H_2O.

Although the promotional effect of water on Pd/Al_2O_3 catalysed CO oxidation reactions has been viewed before, this has primarily been

reported for low-temperature conditions ($< 100\,°C$) [62–65]. Oh et al. have demonstrated that hydroxyl groups play a key role in low temperature CO oxidation reactions, suggesting that adsorbed hydroxyl groups promote CO oxidation by forming either bicarbonate or formate intermediates, which can easily decompose to CO_2 [62]. Parker was unable to observe the formation of either bicarbonate or formate species through inelastic neutron scattering spectroscopy, however was able to identify that two hydroxyl groups are required in the CO oxidation process [63]. In the work of Kwon et al. [64], FTIR vibrational bands corresponding to the formation of carbonate and carboxylate species on Pd were observed, and it was concluded that these species contributed to the promotional effect on the catalyst activity at low temperatures. Caporali et al. demonstrated through isotopic labelling experiments under lean conditions, that the oxidation of CO occurs primarily through reaction with H_2O or hydroxyl groups, and not O_2 [65]. Formate was elucidated as a surface intermediate species, requiring two hydroxyl groups to convert CO into CO_2 which is consistent with the work of Oh et al. and Parker [62,63].

The hypothesized reaction network is summarised in Table 4 and has been derived from the analysis of the spatiotemporal plots in Figs. 12 and 13. Fig. 13(d) details the spatiotemporal carbon atom balance for the wet feed carried out on the non-TWC. From analysis of the plot, regions 5 and 6 corresponding to a time period directly succeeding the switch from rich to lean conditions, exhibit spatiotemporal instances where excess carbon is detected in the gas phase. This excess carbon is indicative of a carbon species deposited earlier in the switching cycle, which is made apparent by the small deficit of gas phase carbon observed during rich conditions in region 4. The excess carbon observed in region 5 is accredited to the formation of CO_2, thought to be as a result of the oxidation of adsorbed carbon species whenever the catalyst environment changes from reducing to oxidizing conditions.

Fig. 13(c) showing the spatiotemporal CO conversion in excess of stoichiometry, indicates less CO conversion in regions 5 and 6 than is predicted by stoichiometric reaction, however both CO_2 yield and O_2 conversion in Fig. 13(b) exceed 100% in regions 5 and 6, therefore the hypothesis holds true. Not only is O_2 removed by reaction with incoming fresh CO in region 5, and adsorbed carbon species in regions 5 and 6, but also H_2 formed under rich conditions in region 3. Fig. 13(a) detailing the CO conversion brought about by the WGSR, has been predicted via the observed H_2 formed, and it is noted that the H_2 formed is able to persist under the predicted lean conditions in region 6, suggesting that sufficient quantities of deposited carbon species and H_2 are available to react with and remove all of the excess O_2 present during lean conditions. Therefore it can be deduced that the catalyst surface is reduced in region 6.

At axial positions after region 6 i.e. towards the back of the tested region (~40 mm), H_2 ceases to exist or be formed due to the complete CO conversion experienced under rich conditions, demonstrated by Fig. 13(c). The deficit of CO conversion experienced in region 5 also suggests that there is a degree of competition between the deposited carbon species, H_2 and CO for the available O_2, quite possibly equating to the region where the additional OSC species, OSC_{add} is being formed. A potential route for the formation of OSC_{add} is suspected to originate from the reaction of H_2O with oxidised Pd in a spatiotemporal region where incoming fresh O_2 is in excess of stoichiometry. The large concentration of H_2O present in the feed at all time instances during the lean-rich cycle, means that an abundance of hydroxyl groups is likely to be found on the catalyst surface, therefore the formation of $Pd(OH)_x$ species would not be surprising. Furthermore, it has been previously demonstrated that two hydroxyl groups take part in the promotion of low temperature CO oxidation reactions [61,62], thus it is tempting to hypothesise that the additional OSC species is of the form $Pd(OH)_2$, however further work is required to verify this.

Table 4
Hypothesized reaction network occurring on non-TWC.

Region	Reactions
1	No Reaction due to H_2O inhibition
2	$2CO_{(g)} + O_{2(g)} \leftrightharpoons 2CO_{2(g)} \ CO_{(g)} + PdO_{(s)} \leftrightharpoons Pd_{(s)} + CO_{2(g)}$
3	$2CO_{(g)} + O_{2(g)} \leftrightharpoons 2CO_{2(g)} \ CO_{(g)} + H_2O_{(g)} \rightleftharpoons CO_{2(g)} + H_{2(g)}$
2,3 → 4	$CO_{(g)} + PdO_{(s)} \leftrightharpoons Pd_{(s)} + CO_{2(g)} \ CO_{(g)} + OSC_{add} \leftrightharpoons Pd_{(s)} + CO_{2(g)} + H_2O_{(g)} \ 2CO_{(g)}$
	$\leftrightharpoons C_{(s)} + CO_{2(g)}$
4	No Reaction
5	$C_{(s)} + O_{2(g)} \leftrightharpoons CO_{2(g)} \ 2CO_{(g)} + O_{2(g)} \leftrightharpoons 2CO_{2(g)} \ O_{2(g)} + 2H_{2(g)} \leftrightharpoons 2H_2O_{(g)}$
6	$CO_{(g)} + H_2O_{(g)} \rightleftharpoons CO_{2(g)} + H_{2(g)}$
7	$O_{2(g)} + 2H_{2(g)} \leftrightharpoons 2H_2O_{(g)} \ O_{2(g)} + 2Pd_{(s)} \leftrightharpoons 2PdO_{(s)}$

4. Conclusions

We have developed and validated an experimental lean-rich cycling methodology capable of spatially and temporally resolving reaction profiles occurring inside washcoated monolith cores. Evidence of important processes including carbon deposition, preferential utilization of OSC and re-oxidation process have been observed and used to hypothesize the reaction pathways occurring for CO oxidation reactions, both in the presence and absence of H_2O in the feed. Interestingly, in the presence of H_2O, the $3\%Pd/Al_2O_3$ washcoated monolith core was shown to exhibit a behaviour similar to that of an OSC containing catalyst, especially under rich conditions, where excess CO conversion, in addition to the WGSR was observed. Many surface species (including formate, bicarbonate, carbonate or carboxylate) have been hypothesized as potential CO oxidation promoters in literature, however the experimental evidence in this work suggest that a non-carbon based surface species is responsible for the additional OSC observed under rich conditions, most likely $Pd(OH)_2$.

Appendix A. Supplementary data

Supplementary material related to this article can be found, in the online version, at doi:https://doi.org/10.1016/j.apcatb.2019.117918.

References

[1] (a) W.P. Partridge, J.S. Choi, Exhaust aftertreatment gas phase measurements in situ, 6th diesel engine emissions reduction workshop, DEER (August 23) (2000); (b) G. Kalghatgi, B. Johansson, Proc. IMechE Part D: J. Automobile Eng. 232 (1) (2018) 118–138.
[2] S. Sillman, Atmos. Environ. 33 (1999) 1821.
[3] E.N. Allred, E.R. Bleecker, B.R. Chaitman, T.E. Dahms, S.O. Gottlieb, J.D. Hackney, Res. Rep. Health Eff. Inst. 25 (1989) 1.
[4] R.M. Heck, R.J. Farrauto, S.T. Gulati, Catalytic Air Pollution Control: Commercial Technology, 3rd ed., John Wiley & Sons, Inc, Hoboken, New Jersey, 2009.
[5] S.A. Ciatti, Front. Mech. Eng. 1 (2015) 5.
[6] EC, "Dir ective 2008/50/ EC of the European parliament and of the council of 21 May 2008 on ambient air quality and cleaner air for Europe", Off. J. Eur. Union (2008) L152/1.
[7] EC, "dir ective 2009/28/ EC of the European parliament and of the council of 23 April 2009 on the promotion of the use of energy from renewable sources and amending and subsequently repealing dir ectives 2001/77/ EC and 2003/30/ EC", Off. J. Eur. Union (2009) L140/16-62.
[8] T.V. Johnson, SAE Int. J. Engines 8 (2015) SAE Paper no. 2015-01-0993.
[9] E.E.A. Report, Electric Vehicles in Europe, Publications Office of the European Union, Luxembourg, 2016.
[10] K. Morgan, A. Goguet, C. Hardacre, ACS Catal. 5 (2015) 3430.
[11] M.V. Twigg, Platinum Met. Rev. 42 (1999) 168.
[12] P.L. Silveston, Catal. Today 25 (1995) 175.
[13] Z. Han, J. Wang, H. Yan, M. Shen, J. Wang, W. Wang, M. Yang, Catal. Today 158 (2010) 481.
[14] J. Barbier, D. Duprez, Appl. Catal., B 4 (1994) 105.
[15] J. Pérez-Ramírez, E.V. Kondratenko, Catal. Today 121 (2007) 160.
[16] J.T. Gleaves, G.S. Yablonskii, P. Phanawadee, Y. Schuurman, Appl. Catal., A 160 (1997) 55.
[17] H. Santos, M. Costa, Energy Convers. Manag. 49 (2008) 291.
[18] C.N. Montreuil, S.C. Williams, A.A. Adamczyk, SAE Paper No. 920096, (1992).
[19] K. Ueda, J. Ohyama, A. Satsuma, ACS Omega 2 (2017) 3135.
[20] S. Tagliafeti, R.A. Koppel, A. Baiker, Appl. Catal. B 15 (1998) 159.
[21] H.C. Yao, Y.F. Yu Yao, J. Catal. 86 (1984) 254.
[22] T. Miki, T. Ogawa, M. Haneda, N. Kakuta, A. Ueno, S. Tateishi, S. Matsuura, M. Sato, J. Phys. Chem. 94 (1990) 6464.
[23] R. Taha, D. Martin, S. Kacimi, D. Duprez, Catal. Today 29 (1996) 89.
[24] S. Bedrane, C. Descorme, D. Duprez, Catal. Today 75 (2002) 401.
[25] P.S. Lambrou, C.N. Costa, S.Y. Christou, A.M. Efstathiou, Appl. Catal. B 54 (2004) 237.
[26] J.T. Gleaves, G. Yablonsky, X. Zheng, R. Fushimi, P.L. Mills, J. Mol. Catal. A: Chem. 315 (2010) 108.
[27] K. Morgan, N. Maguire, R. Fushimi, J.T. Gleaves, A. Goguet, M.P. Harold, E.V. Kondratenko, U. Menon, Y. Schuurman, G.S. Yablonsky, Catal. Sci. Technol. 7 (2017) 2416.
[28] C. Ledesma, J. Yang, D. Chen, A. Holmen, ACS Catal. 4 (2014) 4527.
[29] K. Morgan, J. Touitou, J.S. Choi, C. Coney, C. Hardacre, J.A. Pihl, C.E. Stere, M.Y. Kim, C. Stewart, A. Goguet, W.P. Partridge, ACS Catal. 6 (2016) 1356.
[30] A. Baiker, D. Epple, Appl. Catal. 22 (1986) 55.
[31] A. Baiker, M. Bergougnan, Can. J. Chem. Eng. 63 (1985) 138.
[32] J. Touitou, K. Morgan, R. Burch, C. Hardacre, A. Goguet, Catal. Sci. Technol. 2 (2012) 1811.
[33] J. Touitou, R. Burch, C. Hardacre, C. McManus, K. Morgan, J. Sa, A. Goguet, Analyst 138 (2013) 2858.
[34] J. Touitou, F. Aiouache, R. Burch, R. Douglas, C. Hardacre, K. Morgan, J. Sa, C. Stewart, J. Stewart, A. Goguet, J. Catal. 319 (2014) 239.
[35] C. Stewart, E.K. Gibson, K. Morgan, G. Cibin, A. Dent, C. Hardacre, E.V. Kondratenko, V. Kondratenko, C. McManus, S. Rogers, C.E. Stere, S. Chansai, T.C. Wang, S. Haigh, P.P. Wells, A. Goguet, ACS Catal. 8 (2018) 8255.
[36] W.P. Partridge, J.M.E. Storey, S.A. Lewis, R.W. Smithwick, G.L. DeVault, M.J. Cunningham, N.W. Currier, T.M. Yonushonis, SAE Trans: J. Fuels Lubricants. 109 (2000) 2992.
[37] J. Sa, D.L. Fernandes, F. Aiouache, A. Goguet, C. Hardacre, D. Lundie, W. Naeem, P. Partridge, C. Stere, Analyst 135 (2010) 2260.
[38] O. Shakir, A. Yezerets, N.W. Currier, W.S. Epling, Appl. Catal. A 365 (2009) 301.
[39] J.Y. Luo, X. Hou, P. Wijayakoon, S.J. Schmieg, W. Li, W.S. Epling, Appl. Catal. B 102 (2011) 110.
[40] X. Hou, S.J. Schmieg, W. Li, W.S. Epling, Catal. Today 197 (2012) 9.
[41] R. Horn, K.A. Williams, N.J. Degenstein, L.D. Schmidt, J. Catal. 242 (2006) 92.
[42] M. Bosco, F. Vogel, Catal. Today 116 (2006) 348.
[43] J. Kopyscinski, T.J. Schildhauer, F. Vogel, S.M.A. Biollaz, A. Wokaun, J. Catal. 271 (2010) 262.
[44] C. Diehm, H. Karadeniz, C. Karakaya, M. Hettel, O. Deutschmann, Adv. Chem. Eng. 45 (2014) 41.
[45] M. Roos, J. Bansmann, D. Zhang, O. Deutschmann, R.J. Behm, J. Chem. Phys. 133 (2010) 1.
[46] M. Johansson, J. Hoffmann Jørgensen, I. Chorkendorff, Rev. Sci. Instrum. 75 (2004) 2082.
[47] G.S. Bugosh, V.G. Easterling, I.A. Rusakova, M.P. Harold, Appl. Catal. B 165 (2015) 68.
[48] M. Hettel, C. Diehm, B. Torkashvand, O. Deutschmann, Catal. Today 216 (2013) 2.
[49] D. Chan, S. Tischer, J. Heck, C. Diehm, O. Deutschmann, Appl. Catal. B 156 (2014) 153.
[50] H. Nguyen, M.P. Harold, D. Luss, Chem. Eng. Journal 262 (2015) 464.
[51] Y. Liu, M.P. Harold, D. Luss, Appl. Catal. A 397 (2011) 35.
[52] J. Sa, C. Stere, A. Goguet, SpaciMS-probing the internal behaviour of 3D structured materials, in: R. Dias, A.A. Martins, R. Lima, T.M. Mata (Eds.), Single and Two-Phase Flows on Chemical and Biomedical Engineering, Bentham Science Publishers, Portugal, 2012, pp. 3–25.
[53] J. Stewart, R. Douglas, A. Goguet, C. Stere, Can. J. Chem. Eng. 92 (2014) 1535.

[54] A. Goguet, W.P. Partridge, F. Aiouche, C. Hardacre, K. Morgan, C. Stere, J. Sá, Catal. Today 236 (2014) 206.
[55] E.M. Cordi, J.L. Falconer, J. Catal. 162 (1996) 104.
[56] V. Matolin, E. Gillet, Surf. Sci. 238 (1990) 75.
[57] G. Zhou, P.R. Shah, T. Montini, P. Fornasiero, R.J. Gorte, Oxidation Enthalpies for Reduction of Ceria Surfaces, Retrieved from (2007) http://repository.upenn.edu/cbe_papers/94.
[58] T. Bunluesin, R.J. Gorte, G.W. Graham, Appl. Catal. B 15 (1998) 107.
[59] S. Hilaire, X. Wang, T. Luo, R.J. Gorte, J. Wagner, Appl. Catal. A 215 (2001) 271.
[60] R.J. Gorte, S. Zhao, Catal. Today 104 (2005) 18.
[61] K. Fottinger, R. Schlogl, G. Rupprechter, Chem. Commun. 0 (2008) 320.
[62] S.H. Oh, G.B. Hoflund, J. Catal. 245 (2007) 35.
[63] S.F. Parker, Chem. Commun. 47 (2011) 1988.
[64] H.J. Kwon, J.H. Baik, Y.T. Kwon, I.S. Nam, S.H. Oh, Chem. Eng. J. 141 (2008) 194.
[65] R. Caporali, S. Chansai, R. Burch, J.J. Delgado, A. Goguet, C. Hardacre, L. Mantarosie, D. Thompsett, Appl. Catal. B 147 (2014) 764.